A tumor-conditional melittin/atezolizumab safely potentiates the efficacy of anti-PD-L1 immunotherapy through a dual-lock prodrug strategy

Wen Zhu[a], Ying Qin[a], Yuntian Han[a], Gen Qi[a], Qiongya Zeng[a], Zixiang Li[a], Haoran Deng[a], Xinyu Deng[a], Kaijuan Yi[a], Yan Wang[b], Anja Moldenhauer[c], Shanshan Jiang[d,] *, Huili Lu[a,] *

[a] Shanghai Frontiers Science Center for Drug Target Identification and Delivery; Engineering Center for Antibody Drug and Cell Engineering, Ministry of Education; National Key Laboratory of Innovative Immunotherapy; School of Pharmacy, Shanghai Jiao Tong University, 800 Dongchuan Road, Shanghai 200240, China

[b] Department of Geriatrics, Huashan Hospital, Fudan University, 12 Wulumuqi Middle Road, Shanghai 200040, China

[c] Institute for Transplantation Diagnostics and Cell Therapeutics, Heinrich Heine University Dusseldorf, Dusseldorf 40204, Germany

[d] Division of Gastroenterology and Hepatology, Shanghai Institute of Digestive Disease, NHC Key Laboratory of Digestive Diseases, State Key Laboratory of Systems Medicine for Cancer, Renji Hospital, School of Medicine, Shanghai Jiao Tong University, Shanghai 210001, China.

Corresponding author: Dr. Huili Lu, roadeer@sjtu.edu.cn; or Dr. Shanshan Jiang, shanshanjss@163.com

Abstract

Rationale: Although immune checkpoint inhibitors (ICIs) represent a major breakthrough in cancer therapy, limited efficacy and immune-related adverse events (irAEs) substantially restrict their clinical use.

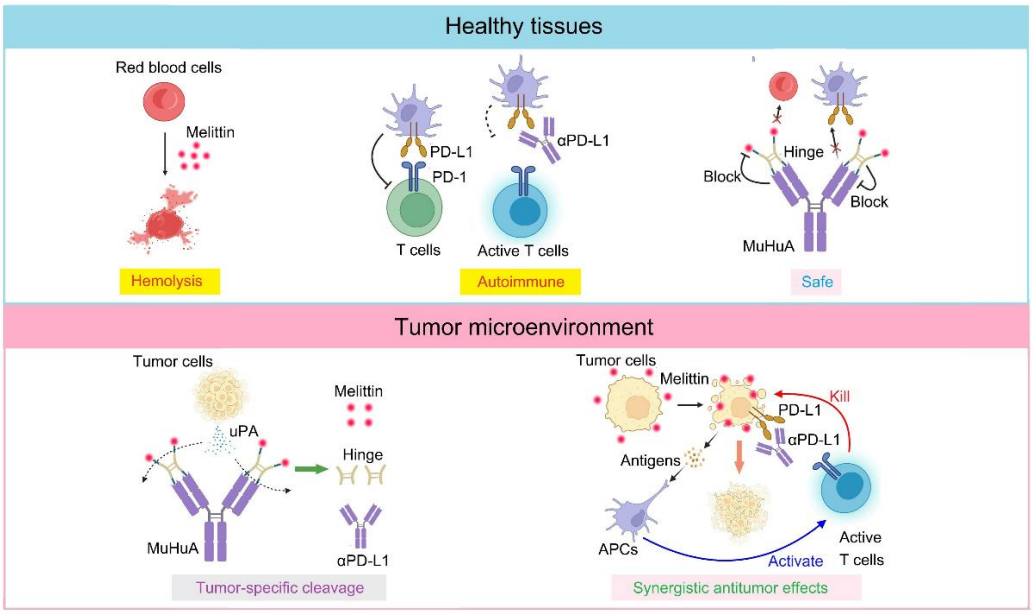
Methods: To address these challenges, we developed MuHuA, a tumor-selective dual-lock prodrug based on atezolizumab. The construct was generated by attaching melittin and a human IgG1 hinge domain to the N terminus of the PD-L1-targeting antibody through a cleavable peptide linker. This integration is achieved via a cleavable peptide linker that is sensitive to tumor-enriched enzymes, blocking the activity of both melittin and atezolizumab thereby enhancing safety. The tumor uptake and safety were monitored. Therapeutic efficacy was evaluated across hot and cold tumor models, including metastatic and refractory models resistant to conventional ICIs treatments. The profiles of tumor infiltrating lymphocytes were further investigated to elucidate the mechanism of action of MuHuA. Furthermore, we explored the combination of MuHuA with EGFR-targeting CAR T therapy.

Results: MuHuA significantly reduces the hemolytic toxicity of melittin and the irAEs of atezolizumab, demonstrating a favorable pharmacokinetic profile and higher tumor uptake. Upon specific cleavage in the tumor microenvironment, MuHuA releases melittin and atezolizumab, which synergistically suppress tumor growth and improve control of metastatic cancer. The antitumor responses are mechanistically supported by the activation of intratumoral $CD8^+$ T cells and NK cells, along with the enhancement of immune memory, thereby overcoming resistance to ICIs. Additionally, when

combined with CAR-T therapy, MuHuA further exhibits superior antitumor efficacy and lower toxicity compared to atezolizumab.

Conclusions: Overall, the dual-lock prodrug MuHuA effectively rejuvenates tumor-infiltrating lymphocytes, achieving significant therapeutic efficacy and safety. Our work presents a groundbreaking approach for developing safer and more effective cancer immunotherapies, with the potential to address the current clinical challenges of existing immunotherapeutic agents.

Graphical abstract



Key words

PD-L1 antibody, Bee venom-derived cytolytic peptide, irAEs, Enhanced antitumor efficacy, Prodrug strategy

Introduction

Inhibitory immune checkpoint inhibitors, such as monoclonal antibodies (mAbs) against programmed cell death protein 1 (PD-1) and its ligand (PD-L1), have proven to be effective strategies for enhancing T cell cytotoxicity in cancer patients [1]. However, these agents frequently trigger a wide range of irAEs due to their role in maintaining immunological homeostasis [2, 3]. Atezolizumab, an extensively used anti-PD-L1 antibody, has been associated with hepatitis, pneumonitis, colitis, and rash in patients [4]. These irAEs usually lead to dose reductions, treatment delays, and discontinuations, significantly hindering successful therapy. On the other hand, the therapy also frequently faces the challenge of primary or acquired drug resistance, which can result in therapeutic failure [5, 6].

Because the therapeutic benefits of immunotherapy are often accompanied by treatment-related toxicities, developing approaches that preserve antitumor efficacy while minimizing adverse effects has become an important objective in anticancer drug development [7-9]. Recent advances in immunotherapy and antibody engineering have increasingly focused on widening the therapeutic window by exerting spatial control to potent immune and cytotoxic activities. Engineered antibody formats, typically prodrugs, provide platforms for improving tumor selectivity, while tumor associated proteases act as endogenous biochemical triggers for conditional activation [10-13]. While remaining largely intact and maintaining a masked state in healthy tissue, an antibody prodrug exhibits a prolonged half-life in the circulatory system. Upon reaching the tumor site, it undergoes cleavage by tumor-specific proteases, which releases the antibodies and enables binding to tumor targets

[14-16]. The prodrug of cetuximab, a therapeutic antibody known for its on-target off-tumor side effects, retained potent tumor inhibition effects while significantly reducing toxicity in nonhuman primates [17]. CX-072, an anti-PD-L1 prodrug, has demonstrated antitumor efficacy comparable to that of other PD-1/PD-L1 inhibitors, while showing a potentially more favorable safety profile (NCT03993379).

However, mitigating toxicity alone does not address the clinical limitations of ICIs, particularly in "cold" tumors with insufficient T cell infiltration. Antitumor effect is highly dependent on the efficient presentation of tumor antigens [18, 19]. In clinical trials, PD-1/PD-L1 blockade can synergize with chemotherapy or radiotherapy, which promotes the release of tumor antigens [20, 21]. Over the last few decades, there has been a significant rise in research on anticancer peptides (ACPs) [22], which can lyse tumor cells and improve antigen exposure [23]. Melittin, a representative lytic toxin, has shown antitumor activity [24]. Direct administration of melittin into colon tumors was reported to decrease tumor volume by approximately 50% [25]. By inducing immunogenic cell death, melittin could potentially mimic the antigen release effects of chemotherapy or radiotherapy, thereby rendering tumors more susceptible to ICI therapy. However, systemic administration of melittin remains infeasible due to hemolytic toxicity and a narrow therapeutic window, despite extensive efforts to improve its delivery using nanocarriers, microcapsules, and liposomes [26, 27]. Nevertheless, nanoparticle-based delivery produced only a modest increase in the median lethal dose (LD50) in mice, accompanied by significant off-target accumulation in the liver [28, 29]. Therefore, for clinical applications, an alternative

approach that enhances melittin stability, minimizes hemolytic damage, and improves tumor-selective delivery must be developed.

In this work, we sought to simultaneously address both the toxicity and efficacy challenges of ICI therapy by combining a tumor-activated prodrug strategy with the antigen-release properties of melittin. We conjugated atezolizumab with an autologous IgG1 hinge domain and linked the entire sequence to the C-terminus of melittin, thus developing a melittin/atezolizumab dual-lock prodrug, termed MuHuA. This molecule can significantly reduce melittin-mediated hemolysis while masking the PD-L1-binding activity of atezolizumab, thereby improving tolerability at higher doses. Upon cleavage by the tumor-associated urokinase-type plasminogen activator (uPA), the prodrug releases melittin and atezolizumab. The released melittin induces immunogenic cell death, releasing tumor antigens and enhancing the antitumor immune response, which synergizes with atezolizumab-mediated PD-L1 blockade. In murine studies, MuHuA exhibited antitumor activity against both immunologically hot and cold tumors. These findings suggest its potential relevance to challenging therapeutic settings, including metastatic disease and advanced cancers that exhibit resistance to ICI therapy. MuHuA treatment also significantly enhances the antitumor efficacy of CAR-T therapy with a favorable safety. Overall, by successfully decoupling antitumor efficacy from systemic toxicity, MuHuA may pave the way for broader clinical applications of ICIs.

Materials and Methods

Cell lines

MC38 murine colon carcinoma cell line, RM-1 murine prostate carcinoma cell line, HT29 human colon cancer cell line, U251 MG human glioblastoma cell line, and HCC1954 human breast cancer cell line were obtained from the American Type Culture Collection (ATCC) and cultured in Dulbecco's Modified Eagle's Medium (DMEM) (Gibco, USA) supplemented with 10% fetal bovine serum (FBS) (Gibco, USA). HEK293E cells were cultured and used for recombinant protein production as previously described [30].

Cloning, expression, and purification

MuHuA was engineered by introducing melittin and multiple linker and protease-cleavable elements at the N-termini of both atezolizumab chains. The amino acid sequences and arrangement of these elements were based on a previously reported design [30]. Briefly, the heavy-chain construct comprised melittin, two uPA-sensitive cleavage sites (LSGRSDNH), the human IgG1 hinge region, and the corresponding linker sequence. These elements were assembled by overlap-extension PCR. The light chain was modified using a corresponding design. From the N-terminus, the construct contained melittin, an LSGRSDNH cleavage sequence, linker-1 (VN), the human IgG1 hinge region, linker-2 (VN), a second LSGRSDNH cleavage sequence, and linker-3 (AAQPA). In other words, each chain of the MuHuA construct contains two uPA-cleavable sites: one positioned between melittin and the hinge region, and the other between the hinge region and atezolizumab. Other constructs designed are illustrated in the manuscript. For MuHu4, the anti-4-1BB agonistic antibody (a4, clone 3H3) was

used. Antibody expression and purification were performed as previously described [30].

Hemolysis and tumor cell cytotoxicity assays

To induce proteolytic cleavage *in vitro*, 90 μg of the fusion protein was exposed to 3 μg of uPA (SinoBiological, China) in PBS at 37 °C for 60 h. To minimize potential interference from incomplete cleavage, the *in vitro* cleavage period was extended to 60 h to ensure complete uPA-mediated processing of MuHuA. Mouse red blood cells were prepared as previously reported [31]. Hemolytic activity of free melittin (Apeptides, China), MuHuA, or cleaved MuHuA was subsequently evaluated using mouse RBCs as previously described [30].

For tumor cytotoxicity assays, 1×10^4 MC38, RM-1, HT29, U251 MG, or HCC1954 cells were plated in 96-well plates and cultured for 12 h before exposure to different concentrations of free melittin, MuHuA, or cleaved MuHuA.

For the uPA specific cytotoxicity assay, 10,000 MC38, RM-1, U251 MG, or MCF-7 cells were distributed into 96-well plates and maintained for 12 h before treatment. The cells were then treated with 0.25 μM MuHuA & uPA or MuHuA & uPA & uPA inhibitor GGACK (Beyotime, China). We pre-cleaved uPA and MuHuA with or without GGACK *in vitro* for 60 h, and then added them to the aforementioned cells. After 8 h of treatment, cell viability was determined using the CCK-8 assay as previously described [30].

Furthermore, uPA was replaced with MMP2, MMP9, cathepsins, legumain, PSA, plasmin, human serum, or mouse serum. The cleavage efficiency was assessed by measuring the restoration of PD-L1 antibody affinity.

For intratumoral uPA activity assessment, MC38 or RM-1 cells were subcutaneously implanted into the right axilla of female or male C57BL/6 mice, respectively. Meanwhile, MCF-7 or U251 MG cells were subcutaneously implanted into the right axilla of female NCG mice. HCC1954 cells were orthotopically implanted into the fourth mammary fat pad of female NCG mice. Once the subcutaneous tumors reached approximately 500 mm^3 and orthotopic tumors reached approximately 200 mm^3, the tumors were excised, and tumor interstitial fluid was collected. Subsequently, uPA concentrations were quantified using mouse- or human-specific uPA ELISA kits (Jingmei Biotechnology, China).

ELISA assay

For the PD-L1 binding assay, 96-well plates (Corning, USA) were coated overnight at 4 °C with mouse PD-L1 (1.0 μg/mL in PBS; Novoprotein, China), followed by blocking with 3% BSA in PBS. The plates were then incubated with the indicated concentrations of atezolizumab, MuHuA, cleaved MuHuA, or cleaved HuA. The data were collected following previously described procedures [32].

Immunofluorescence

RM-1 tumor tissues were processed for cryosectioning within 1 h after excision. Samples were placed in OCT embedding medium, rapidly frozen using liquid nitrogen, and cut into 20-μm-thick sections. After blocking with 3% BSA in PBS, sections were exposed to 1 μg/mL atezolizumab, MHA, MuHuA, or MuHuA combined with 0.1 mM AEBSF or the uPA inhibitor GGACK. Incubation was carried out overnight at 4 °C in Tris-HCl buffer (50 mM, pH 7.4) supplemented with 150 mM NaCl, 100 mM $ZnCl_2$, 5 mM $CaCl_2$, and 0.05% Tween-20. After removal of unbound proteins by washing,

fluorescence detection was performed with a FITC-labeled goat anti-human secondary antibody (Thermo Fisher, USA) for 1 h at room temperature. For evaluation of intratumoral T-cell infiltration, MC38 tumors from the indicated treatment groups were analyzed by immunofluorescence. CD8 and CD4 were examined by dual staining, whereas Foxp3 was assessed on adjacent sections. Nuclear counterstaining was performed with DAPI (Beyotime, China). Fluorescence micrographs were acquired using a Leica SP8 confocal microscope.

Hematoxylin and eosin staining and immunohistochemistry

After transcardiac perfusion with saline, the pancreases of NOD mice, the tumor tissues of C57BL/6 mice, or the liver and mammary gland tissues of NCG mice were resected and stained with rabbit anti-mouse CD45/CD3/Ki67 or rabbit anti-human cleaved caspase 3 antibodies (Servicebio, China) at 4 °C overnight as we described previously [33]. Following primary-antibody staining, HRP-linked goat anti-rabbit IgG (Servicebio, China) was applied for 1 h. Immunoreactivity was subsequently visualized with DAB, followed by hematoxylin counterstaining. Images were acquired using an OLYMPUS BX53 microscope.

RNA isolation and qRT-PCR analysis of mRNA expression

RNA was isolated from the pancreases of NOD mice or tumor tissues collected from C57BL/6 mice using the Ultrapure RNA Kit (Cwbio, China). Reverse transcription was carried out with PrimeScript RT Master Mix (Takara, Japan) to generate cDNA. qRT-PCR was conducted using a 7500 Fast Real-Time PCR System (Thermo Fisher, USA) and Hieff qPCR SYBR Green Master Mix (Yeasen, China). Primer details are given in

Table S2. Gene expression was normalized to GAPDH and quantified by the $2^{\wedge(-\Delta\Delta Ct)}$ method.

Pharmacokinetics and biodistribution studies

Following intravenous administration of 2 mpk hIgG, atezolizumab, or MuHuA, blood was sampled at 1, 2, 6, 12, and 24 h, and then once daily thereafter. For ELISA analysis, 1.0 μg/mL goat anti-human IgG antibody (Beyotime, China) was used to coat the plates overnight at 4 °C. Plasma concentrations of hIgG, atezolizumab, and MuHuA were subsequently determined as previously described [30].

For biodistribution analysis, a single 0.5 mpk dose of atezolizumab or MuHuA was administered intravenously to RM-1 tumor-bearing mice. At 6 days after administration, the animals were euthanized and subjected to transcardial saline perfusion. The tumor and major organs, including the heart, liver, spleen, lung, kidney, mesenteric lymph node, and thymus, together with blood, were harvested. Tissue specimens (20–100 mg) were homogenized in PBS at a ratio of 5 μL/mg, and centrifuged to collect the resulting supernatants. Target protein levels were quantified by ELISA using plates coated with goat anti-human IgG antibody and were normalized to tissue weight. To specifically quantify atezolizumab released from MuHuA, mouse PD-L1 was employed as the coated antigen.

Animal experiments

All animal procedures were approved by the Animal Care and Use Committee of Shanghai Jiao Tong University (Ethics number: 202501162). Sex-matched C57BL/6 mice aged 6–8 weeks were obtained from Shanghai SLAC Laboratory Animal Co., Ltd. and maintained under specific pathogen-free conditions with appropriate animal care.

Groups were balanced by body weight in toxicity studies and by both body weight and tumor volume in efficacy studies. Tumor dimensions were recorded with a digital caliper, and tumor volume was estimated as (length × width^2) / 2. Tumor growth inhibition was calculated as TGI (%) = 100 × (1-T/C), where T and C represent the mean tumor volumes of the treatment and control groups, respectively. Hematological and serum biochemical analyses were performed as previously described procedures [30].

5 × 10^5 MC38 or RM-1 cells suspended in 100 μL PBS were inoculated subcutaneously into the right flank. Treatment allocation was performed on day 10, when tumors had grown to approximately 100 mm^3. MuHuA was administered intravenously at 350 pmol every 4 days in the MC38 model and 1000 pmol every 3 days in the RM-1 model. For synergistic studies, MuHuA was given at 350 pmol every 3 days. For advanced-stage tumors, MuHuA was given at 1000 pmol every 3 days starting when tumors reached ~300 mm^3 (day 14). MuHu4 was administered according to the same dosing schedule.

For the tumor rechallenge experiment, mice received a single intravenous administration of MuHuA at 350 pmol in the MC38 model or 1000 pmol in the RM-1 model. Primary tumors were surgically excised after reaching approximately 300 mm^3, and the incisions were sealed using Vetbond tissue adhesive (3M, USA). At 30 days post-resection, 2.5 × 10^6 MC38 or RM-1 cells were subcutaneously inoculated into the left flank of the corresponding mice. Tumor progression following the second inoculation was assessed by serial volume measurements.

For the *in vivo* uPA inhibition experiment, MuHuA was intravenously administered at 350 pmol every 4 days in MC38 tumor-bearing mice and at 1000 pmol every 3 days in RM-1 tumor-bearing mice. Once tumors reached approximately 100 mm^3 (day 10), the uPA inhibitor GGACK (3 mg/kg) was administered intraperitoneally every two days in both models.

For the orthotopic human breast cancer model, female NCG mice (GemPharmatech, China) aged 6-8 weeks were inoculated with 3×10^6 HCC1954 cells (50% matrigel) into the 4^{th} mammary fat pad. CAR-T cells were generated as previously described using a CAR comprising the EGFR scFv (clone G5V2), which is cross-reactive with both human and mouse EGFR, the CD8 hinge and transmembrane domain, the 4-1BB cytoplasmic domain, and the CD3ζ cytoplasmic domain [34]. Once tumor volumes reached approximately 50 mm^3 on day 7, mice were randomized into the indicated treatment groups. EGFR CAR-T cells (2×10^6) were delivered intravenously on day 7, followed by intravenous MuHuA administration at 1,000 pmol per dose, with injections repeated at 4-day intervals beginning on day 10.

Tumor-specific IFN-γ restimulation assay

The tumor-specific IFN-γ restimulation assay was adapted from our previously reported protocol [30], with modifications to splenocyte preparation. MC38 or RM-1 cells were mitomycin-C-inactivated before co-culture with splenocytes. Splenic single-cell suspensions were prepared using a 200-mesh nylon net followed by RBC lysis. Mitomycin-C-treated tumor cells (2.5×10^4) were then co-cultured with 1×10^6 splenocytes in 200 μL of RPMI 1640 containing 10% FBS, 1×

282 penicillin/streptomycin, and 20 U/mL IL-2. After 72 h, IFN-γ levels in the culture
283 supernatants were quantified using a Mouse IFN-γ ELISA Kit (Multi Sciences, China).

284 **Flow cytometry**

285 Flow cytometric analysis was performed as previously described [30]. The staining
286 panel comprised BV421 anti-mouse CD25 (clone A18246A , BioLegend, Cat#113705),
287 APC anti-Mouse CD8a Antibody (clone S18018E, BioLegend, Cat#162305), FITC
288 Hamster Anti- Mouse CD3e (clone 145–2 C11, BD Pharmingen, Cat#553061), Alexa
289 Fluor 647 anti-mouse FOXP3 (clone MF-14, BioLegend, Cat#126407), PE Rat Anti-
290 Mouse CD4 (clone GK1.5, BD Pharmingen, Cat#557308), APC/Cy7 Rat Anti- Mouse
291 CD45.2 (clone 30- F11, BD Pharmingen, Cat#557659), Fc block- anti- Mouse CD16/32
292 (BioLegend, Cat#101302), Fixable Viability Stain 510 (BD Pharmingen, Cat# 564406).
293 For intracellular FOXP3 detection, cells were subjected to fixation and
294 permeabilization, followed by antibody staining in Perm/Wash buffer for 30 min at 4 °C.
295 Flow cytometric data were acquired with an LSRFortessa™ X-20 Cell Analyzer (BD
296 Biosciences, USA) and subsequently processed in FlowJo software (Tree Star Inc.,
297 Ashland, OR). Fifty thousand events were acquired from blood and spleen specimens,
298 while 100,000 and 200,000 events were acquired from the MC38 and RM-1 tumor
299 samples, respectively.

300 **Statistical analysis**

301 Quantitative data are summarized as mean ± standard deviation (SD). Survival
302 distributions were evaluated with the Mantel–Cox log-rank test. For comparisons of
303 other datasets, either an unpaired two-sided Student's *t*-test or one-way analysis of
304 variance (ANOVA) was applied, as appropriate. Statistical calculations were carried

out in GraphPad Prism 7.0. Differences were considered statistically significant at $p < 0.05$, with significance levels denoted as follows: $p < 0.05$ (*), $p < 0.01$ (**), and $p < 0.001$ (***).

Results

Design of the Melittin/Atezolizumab dual-lock prodrug

We generated MuHuA as a dual-lock prodrug combining melittin with atezolizumab. Its molecular architecture incorporates melittin (M), a human IgG1 hinge region (H), and two uPA-responsive cleavage linkers (u) at the N-terminal ends of the atezolizumab heavy and light chains (A). Based on the design, the hinge domain is intended to block the activity of atezolizumab, while the hinge domain together with atezolizumab blocks the activity of melittin (Figure 1A). This design aims to allow MuHuA to retain its antitumor activity while minimizing systemic toxicity.

The MuHuA structure was modeled with AlphaFold 3 (Figure 1B), and the predicted conformation was consistent with the designed architecture. SDS-PAGE revealed that uPA treatment resulted in the release of melittin and atezolizumab from MuHuA, whereas no corresponding release was observed for the non-cleavable MHA lacking the uPA-cleavable linkers (Figure 1C).

MuHuA blocks melittin activity *in vitro* and releases it upon specific cleavage

To validate that the hemolytic activity of melittin in MuHuA can be quenched, we conducted a hemolytic assay using mouse RBCs. While free chemically synthesized melittin effectively induced RBC lysis, the lysis activity was completely abolished for

MuHuA (Figure 1D and S1A). We further examined the restoration of lytic activity of MuHuA after protease cleavage in the tumor microenvironment (TME). We observed that uPA cleavage efficiently released melittin from MuHuA, restored its activity, and lysed multiple tumor cell lines, including the murine MC38 and RM-1 cells (Figure 1E), and the human HT29 and U251 MG cells (Figure S1B), with activity comparable to that of the free melittin.

To further verify the cytotoxicity is mediated by uPA-dependent cleavage, we assessed the restoration of MuHuA lytic activity upon treatment with uPA alone or uPA & uPA inhibitor. The specific uPA inhibitor GGACK completely abolished MuHuA activity by blocking uPA enzymatic activity and thereby preventing MuHuA cleavage (Figure S2A). MuHuA was efficiently cleaved only in the presence of uPA, whereas it remained stable in the presence of other proteases and in both human and mouse serum. (Figure S2B). What's more, ELISA-based analysis of intratumoral protease levels revealed considerable uPA expression across all five solid tumor models tested (15-65 ng/mg tumor tissue), approaching or exceeding the uPA concentrations used in our *in vitro* assays (about 30 ng/mg), thereby supporting efficient MuHuA cleavage *in vivo* (Figure S2C). These results demonstrate that MuHuA effectively masks the peripheral hemolytic toxicity of melittin, while its intratumoral cytotoxic activity depends on uPA-mediated cleavage.

MuHuA mitigates toxicity of melittin *in vivo*

To determine whether MuHuA attenuates melittin-associated systemic toxicity *in vivo*, C57BL/6 mice received intravenous administration of PBS, 4 nmol melittin (0.5 mpk),

or 1 nmol MuHuA (7.6 mpk) containing 4 nmol melittin, as shown in Figure 1F. Compared with the other groups, free melittin caused a pronounced loss of body weight (Figure 1G) together with obvious physical wasting. Additionally, free melittin also significantly reduced RBC count (Figure 1H) and hemoglobin levels, increased platelet count (Figure S1C), and induced hepatic injury, as reflected by increased serum alanine aminotransferase (ALT) and aspartate aminotransferase (AST) levels (Figure 1I). By comparison, the MuHuA-treated mice showed no evident differences from the PBS group. We further investigated the toxicity of melittin and MuHuA at a higher dose, each containing 12 nmol of melittin, and monitored survival (Figure 1J). Mice treated with melittin showed 100% mortality within 2 days, whereas no death occurred in the MuHuA-treated group (Figure 1K). These results suggest that MuHuA has minimal hemolytic toxicity and holds promise for clinical application.

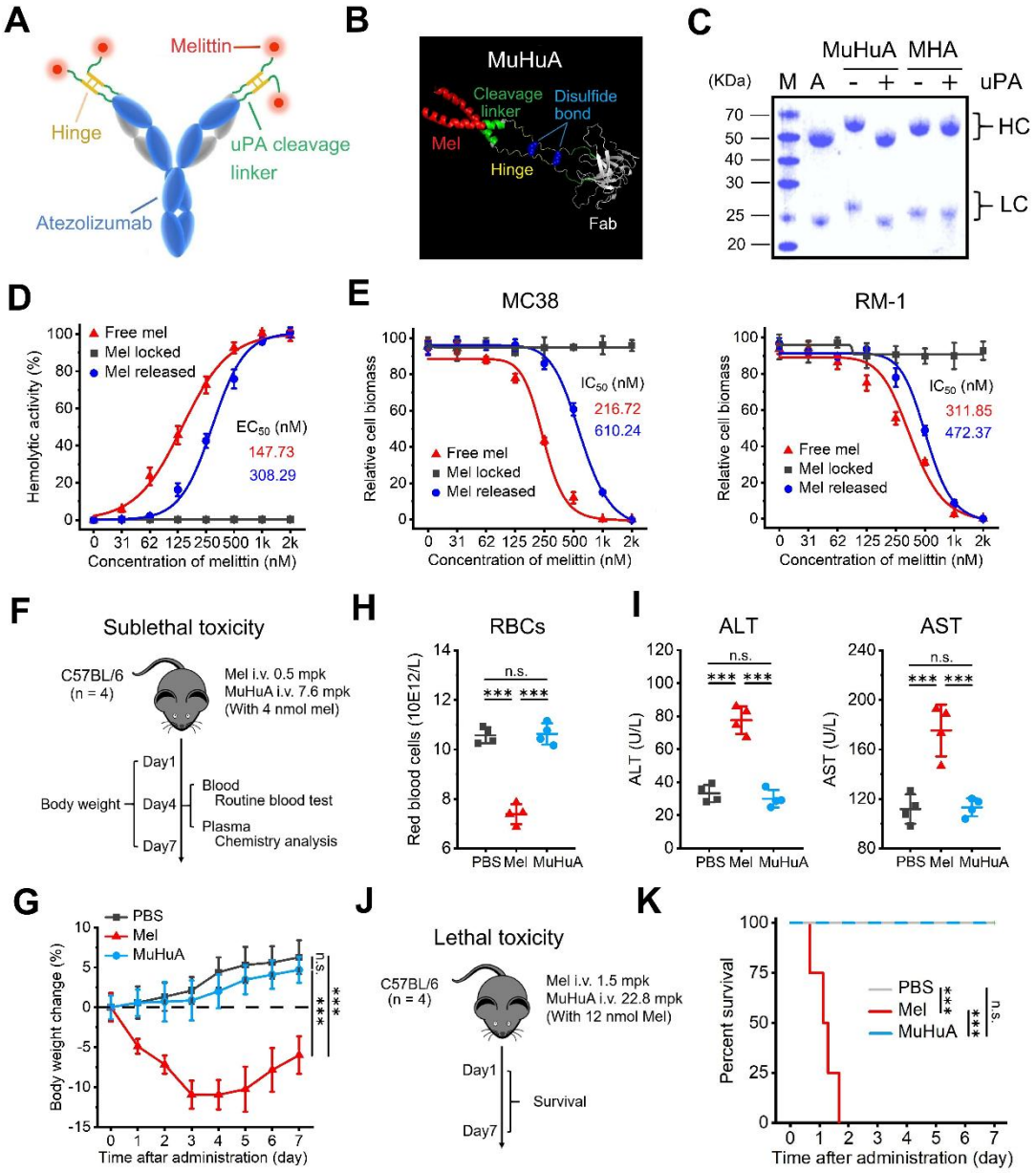


Figure 1. MuHuA reversibly blocks melittin activity *in vitro* and abrogates hemolytic toxicity *in vivo*. (A) Architecture of MuHuA prodrug, with melittin and the human IgG1 hinge domain linked to the N termini of the atezolizumab heavy and light chains through two uPA-cleavable sequences. (B) Structure of MuHuA predicted by AlphaFold 3. (C) Reducing SDS-PAGE analysis of atezolizumab, MuHuA, and MHA, as well as uPA-cleaved MuHuA and MHA (A: atezolizumab; HC: heavy chain; LC: light chain). (D) Mouse RBC lysis induced by free melittin, MuHuA-masked melittin,

or melittin liberated after cleavage (n = 3). (E) Lytic activity of free mel, mel locked in MuHuA, and mel released from MuHuA against MC38 (left) and RM-1 cells (right) (n = 3). (F) Experimental scheme for sublethal toxicity. Drugs were administered on day 0. (G) Body mass was recorded each day after dosing. (H and I) Peripheral blood was obtained 4 days after treatment. RBC abundance was determined by routine hematological analysis (H), whereas serum ALT (I, left) and AST (I, right) were quantified by clinical chemistry testing. (J) Experimental scheme for lethal toxicity study. Drugs were administered on day 0. (K) Survival was monitored after injection. Data are expressed as mean ± SD. *$p < 0.05$, **$p < 0.01$, ***$p < 0.001$; n.s., not significant. Comparisons were performed using an unpaired two-sided Student's *t*-test, whereas survival differences were examined using the Mantel–Cox log-rank test.

MuHuA reversibly masks the PD-L1-binding ability of atezolizumab

To evaluate the masking effect on atezolizumab, we compared the PD-L1-binding activities of atezolizumab and MuHuA using ELISA. The half-maximal effective concentration (EC_{50}) values for atezolizumab and MuHuA were 0.08 nM and 106.31 nM, respectively, indicating that MuHuA exhibits an approximately 1000-fold lower PD-L1-binding ability than atezolizumab (Figure 2A). The binding profile of uPA-cleaved MuHuA was comparable to that of atezolizumab, demonstrating full restoration of PD-L1 affinity following mask removal. Additionally, the similar PD-L1-binding affinities of HuA and MuHuA suggest that the blocking effect on atezolizumab is entirely attributed to the hinge domain.

To further assess whether tumor tissue could activate MuHuA, the proteins were incubated with frozen tumor sections derived from the RM-1 cell line, which secretes high levels of uPA. Compared to the negative staining for non-cleavable MHA, a positive signal was observed in the tumor tissues incubated with atezolizumab and MuHuA. Moreover, MuHuA binding was abolished in tissue sections pre-treated with the uPA-specific inhibitor GGACK, providing additional evidence that proteolytic processing is required to activate MuHuA (Figure 2B).

MuHuA mitigates irAEs associated with PD-L1 blockade

Non-Obese Diabetic (NOD) mice are genetically predisposed to develop T-cell-mediated type 1 diabetes at a young age, making them a valuable model for studying irAEs [35]. Nine-week-old female NOD mice were administered a single intravenous injection of PBS, atezolizumab (400 pmol, 3 mpk), or MuHuA (400 pmol, 3.58 mpk) (Figure 2C). Blood glucose levels were monitored daily using a glucose test strip, and mice with blood glucose levels ≥ 13.88 mmol/L were designated as diabetic. Early-onset diabetes developed in all mice treated with atezolizumab, but no mice in the MuHuA or PBS groups became diabetic (Figure 2D). In addition to excessive thirst and increased urination (data not shown), mice in the atezolizumab group exhibited increased immune cell infiltration (Figure 2E) and elevated levels of inflammatory cytokines in the pancreas, which were not observed in the MuHuA or PBS groups (Figure 2F). These findings demonstrate that MuHuA effectively prevents PD-L1 blockade-induced lymphocyte activation and exacerbation of autoimmune disorders, highlighting its profound safety profile.

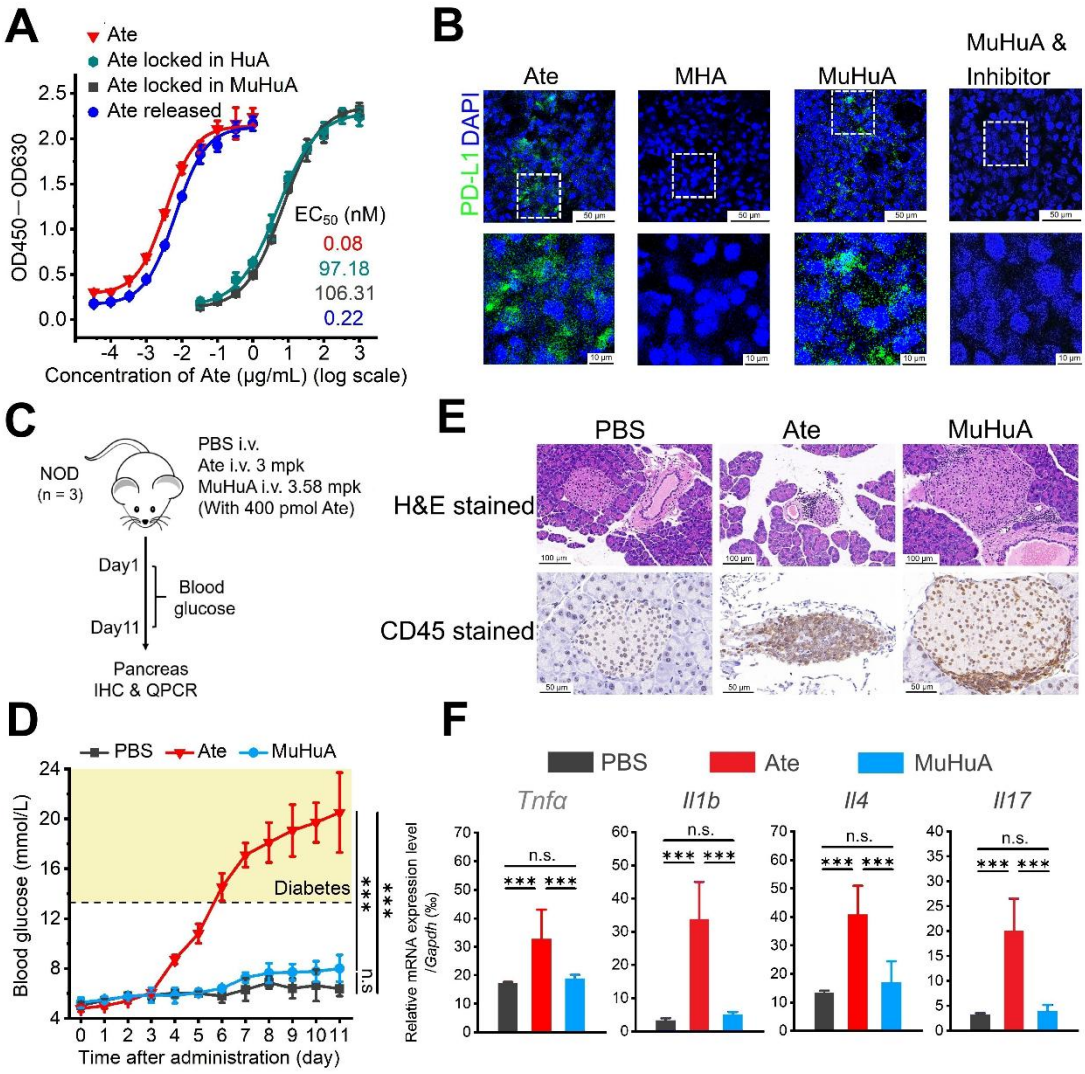


Figure 2. MuHuA reversibly blocks atezolizumab binding to PD-L1 and reduces irAEs. (A) Binding of atezolizumab (Ate), Ate locked in HuA, Ate locked in MuHuA, and Ate released from MuHuA to plate-bound mouse PD-L1 was detected by ELISA (n = 3). (B) *In vitro* restoration of PD-L1 binding in frozen RM-1 tumor xenograft sections. Positive staining was detected by IF in sections incubated with parental Ate or MuHuA, but not with MHA, or MuHuA in the presence of protease inhibitor. Scale bars, 50 μm for overview images and 10 μm for magnified images. (C) Experimental scheme for NOD mouse spontaneous diabetes model. (D) Blood glucose levels were monitored daily after injection. Mice with blood glucose levels ≥ 13.88 mmol/L were designated as diabetic. (E and F) Pancreatic tissues were collected on day 11 post-injection and

analyzed by H&E staining (E). Scale bars, 100 μm for H&E-stained sections and 50 μm for CD45-stained sections. Expression levels of several inflammation-related cytokines in the pancreas were measured using quantitative real-time PCR (F). Data are expressed as mean ± SD. *$p < 0.05$, **$p < 0.01$, ***$p < 0.001$; n.s. indicates no statistical significance. Group comparisons were evaluated using an unpaired, two-sided Student's *t*-test.

MuHuA enhances tumor targeting and tissue biodistribution through the masking strategy

To assess the impact of masking on MuHuA disposition, C57BL/6 mice received intravenous doses of hIgG, atezolizumab, or MuHuA at 2 mpk. Plasma levels of the administered proteins were subsequently quantified from collected blood samples (Figure 3A).

MuHuA showed a distribution half-life ($T_{1/2\alpha}$) and area under the curve (AUC) comparable to those of the hIgG group, while atezolizumab exhibited a shorter $T_{1/2\alpha}$ and lower AUC (Figure 3B and Table S1). The results suggest that atezolizumab can be sequestered by organs enriched in PD-L1-expressing immune cells, such as the spleen, thereby leading to off-target immune stimulation, whereas MuHuA can avoid these off-target side effects.

We further traced tissue distribution in C57BL/6 mice bearing subcutaneous RM-1 tumors treated with atezolizumab or MuHuA (0.5 mpk) by collecting multiple tissues on day 6 (Figure 3C). ELISA quantification demonstrated several-fold lower uptake for MuHuA compared to atezolizumab in lymphoid tissues, including the spleen,

mesenteric lymph nodes, and thymus (Figure 3D, left). In contrast, MuHuA levels were higher in the blood and highly perfused organs, such as the heart, lung, and liver, consistent with its improved pharmacokinetic profile. More importantly, MuHuA reached an approximately threefold higher concentration in tumors than atezolizumab (Figure 3D, right). Within tumors, MuHuA released active atezolizumab to a level comparable to that of the parental antibody, whereas the released atezolizumab was barely detectable in normal tissues (0.7 ng/g in liver, 0.3 ng/g in kidney, and undetectable in blood, heart, spleen, lung, mesenteric lymph node, and thymus). In conclusion, the masking strategy of MuHuA reduces sequestration in PD-L1-expressing lymphoid organs while enhancing preferential accumulation and local activation within the TME.

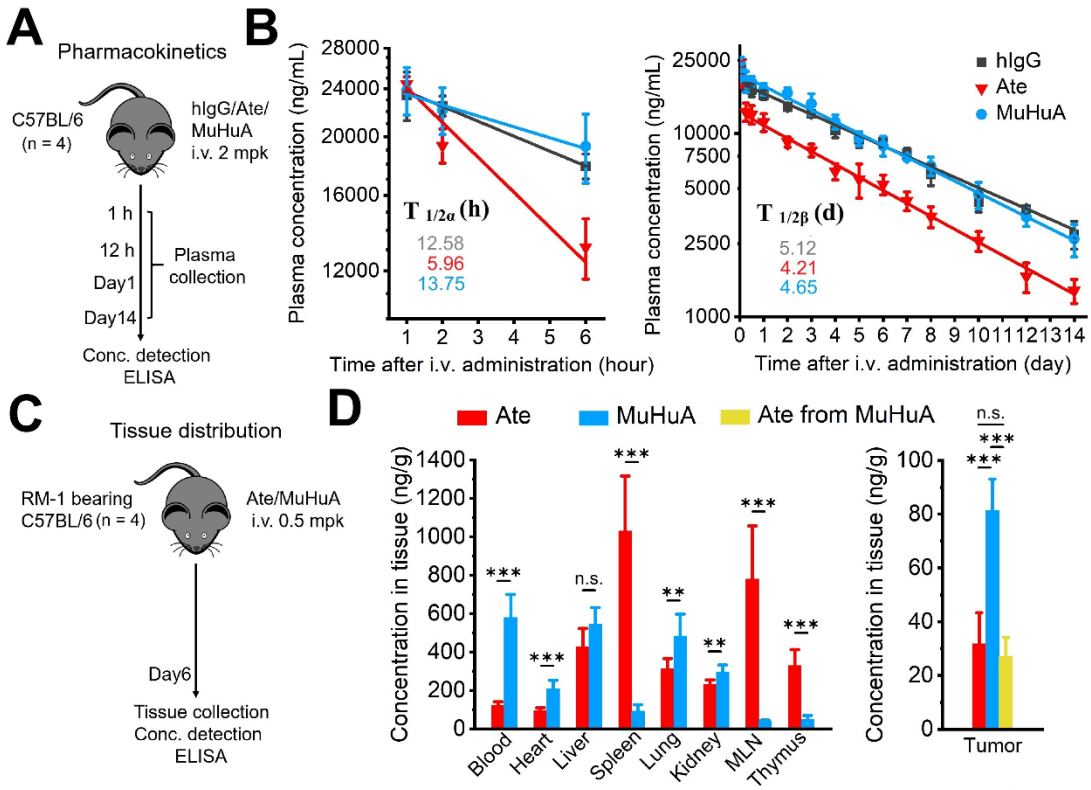


Figure 3. Improved pharmacokinetics profile and tissue distribution of MuHuA.

(A) Experimental scheme for pharmacokinetics. (B) The plasma concentrations of hIgG,

464 atezolizumab (Ate), and MuHuA during the distribution (left) and elimination (right)
465 phase were measured by ELISA. (C) Experimental scheme for tissue distribution. (D)
466 The tissue concentrations of Ate, MuHuA, and Ate released from MuHuA in normal
467 organs (left) and tumors (right) were detected by ELISA.
468
469 **MuHu4 demonstrates the necessity of masking antibody activity**
470 To further investigate the necessity of masking antibody activity, we developed a new
471 construct, MuHu4, which releases both melittin and a 4-1BB agonistic antibody upon
472 uPA-mediated cleavage. Because systemic immune toxicity, especially liver injury, has
473 constrained the therapeutic development of 4-1BB agonists, we incorporated the hinge
474 domain to confine antibody activity within the TME [30, 36-38]. To assess MuHu4
475 efficacy and tolerability, we tested the construct in both MC38 and RM-1 tumor-bearing
476 mice. MuHu4 significantly inhibited tumor growth compared to the 4-1BB antibody
477 alone in both tumor models (Figure S3A-F). Furthermore, MuHu4 did not cause
478 significant body weight loss and markedly alleviated the enlargement of the spleen and
479 inguinal lymph nodes (ILNs) observed following systemic 4-1BB agonist treatment
480 (Figure S3G and S3H). Additionally, MuHu4 significantly reduced serum ALT and
481 IFN-γ levels, indicating attenuated systemic immune activation and 4-1BB agonist-
482 associated hepatotoxicity. Consistently, histological analysis of the liver showed
483 reduced tissue injury, while spleen sections revealed alleviated splenic abnormalities,
484 further supporting the improved systemic safety profile of MuHu4 (Figure S3I and S3J).
485 These findings indicate the necessity of hinge domain mediated masking of antibody
486 activity in our design.

MuHuA controls tumor growth in the MC38 model with minimal toxicity

We initially tested MuHuA in the immunologically inflamed MC38 colon carcinoma setting (Figure 4A). Atezolizumab showed a 31% tumor growth inhibition (TGI), whereas free melittin, either alone or in combination with atezolizumab, unexpectedly promoted tumor growth (Figure 4B and S4A). In contrast, an equimolar dose of MuHuA (350 pmol, 3 mpk) exhibited more potent antitumor activity (70% TGI) and prolonged survival (Figure 4C, median survival: 34 days for MuHuA v.s. 28 days for Ate). This benefit was not observed in the MHA group, indicating that the efficacy was mediated by protease-dependent activation.

Mice treated with MuHuA showed blood routine parameters comparable to those of the hIgG group, while free melittin caused lower RBC count (Figure 4D), lower hemoglobin levels, and higher platelet count (Figure S4B). Flow cytometry (FCM) and immunohistochemical analysis were used to evaluate intratumoral immune responses (Figure S5A). MuHuA treatment resulted in a marked enrichment of tumor-infiltrating lymphocytes, including total T cells, $CD8^+$ T cells, and NK cells (Figure 4E-G, S5B, and S5C). Increased $CD8^+$ T-cell frequencies were also detected in peripheral blood and spleen (Figure 4H, 4I, and S6A-D), with the highest levels observed in the MuHuA group. These findings suggest that $CD8^+$ T cells activated within the tumor may subsequently disseminate through the circulation and accumulate in the spleen. White blood cell counts were comparable among groups (data not shown), but free melittin significantly reduced the frequency of TILs (Figure S7A and S7B). Considering that low RBC levels may impair oxygen delivery, we assessed tumor hypoxia by measuring hypoxia-inducible factor 1α (HIF1α) mRNA levels. The elevated hypoxia levels

indicated that intravenous free melittin injection induced hemolysis and impaired oxygen supply to the tumor, potentially leading to intratumoral immune cell dysfunction and enhanced tumor growth (Figure S7C). These *in vivo* experiments demonstrate that MuHuA can circumvent systemic toxicity associated with hemolysis while enhancing tumor-specific immunity.

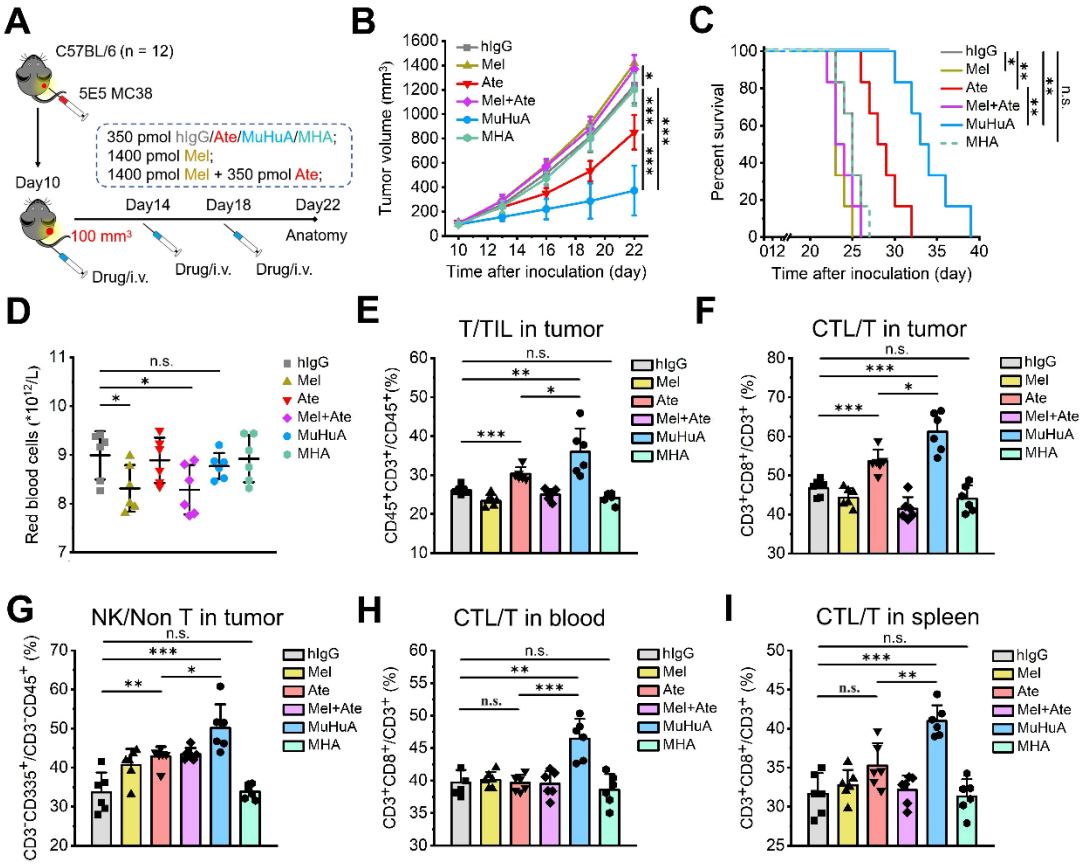


Figure 4. MuHuA suppresses MC38 tumor growth with limited systemic toxicity. (A) MC38 hot-tumor study layout. Tumor growth was monitored in 12 mice. At the control-group endpoint, 6 mice were allocated for tumor weight measurement and flow cytometry, while the remaining animals were followed for survival. (B and C) Longitudinal tumor volume (B) and survival outcome (C), with 1500 mm³ used as the endpoint. (D) Peripheral blood was obtained at the endpoint. RBC counts were measured by routine blood test. (E-G) Tumor-derived single-cell preparations were

analyzed by FCM to determine the proportions of T cells ($CD3^+$) within the $CD45^+$ lymphocyte population (E), $CD8^+$ T cells among $CD45^+CD3^+$ T-cell population (F), and NK cells ($CD335^+$) within the $CD45^+CD3^-$ non-T-cell population (G) were detected by FCM. (H-I) Endpoint blood and spleen lymphocytes were analyzed for $CD8^+$ T-cell frequencies within the T-cell compartment. Data are expressed as mean ± SD. $*p < 0.05$, $**p < 0.01$, $***p < 0.001$; n.s. indicates no statistical significance. Group comparisons were evaluated using an unpaired, two-sided Student's *t*-test. The log-rank (Mantel-Cox) test was used to assess survival.

MuHuA overcomes ICIs resistance in cold tumors with profound safety

Then we evaluated the antitumor efficacy of MuHuA in a typical immune-excluded cold tumor model, an RM-1 cancer model (Figure 5A), which exhibited strong resistance to high-dose atezolizumab treatment (1 nmol, 7.5 mpk) (Figure 5B). However, an equimolar dose of MuHuA (1 nmol, 8.5 mpk) effectively suppressed tumor growth by 46% TGI (Figure 5B and S8A) and improved survival (Figure 5C, median survival: 20 days for MuHuA-L (low dose, 350 pmol), 21 days for MuHuA-H (high dose, 1 nmol), and 19 days for Ate). Importantly, MuHuA at this dose caused no body weight loss (Figure S8B), no significant changes in hemoglobin, platelet count (Figure S8C), or RBC count (Figure 5D), supporting the good tolerability of MuHuA. Flow-cytometric profiling (Figure S9A) showed that lymphocytes and T cells frequencies in RM-1 tumors were markedly lower than those in MC38 tumors. Whereas atezolizumab produced no significant changes relative to hIgG, high-dose MuHuA resulted in a more than twofold enrichment of intratumoral T-cell populations (Figure 5E, S9B, and S9C),

546 and significantly enhanced the infiltration together with greater $CD8^+$ T cells activation
547 (Figure 5F and S9B) as well as NK cells (Figure 5G and S9B). Collectively, there were
548 notably higher numbers of intratumoral $CD8^+$ T cells after MuHuA treatment relative
549 to atezolizumab (11 vs. 2 per thousand total tumor cells). Increased proportions of
550 circulating $CD8^+$ T cells (Figure 5H and S6E) as well as NK cells (Figure 5I and S6F)
551 were also observed in the MuHuA groups, but not in the atezolizumab group.
552 To further assess the therapeutic potential of MuHuA against advanced tumors,
553 treatment was initiated only after MC38 tumors had reached approximately 300
554 mm^3 before treatment (Figure S8D). MuHuA at 1000 pmol significantly inhibited
555 tumor growth, whereas an equimolar dose of atezolizumab showed almost no efficacy
556 (Figure S8E and S8F). MuHuA-treated mice also exhibited prolonged survival (Figure
557 S8G). In addition, MuHuA notably promoted the accumulation of $CD8^+$ T cells within
558 tumors (Figure S8H) and CD335 expression on intratumoral NK cells (Figure S8I).
559 Finally, tumors receiving MuHuA displayed markedly lower Ki67 expression (Figure
560 S8J), indicating suppressed tumor cell proliferation and metastatic potential. These data
561 suggest that MuHuA can effectively control ICI-resistant cold tumors and advanced-
562 stage large tumors with good tolerance.

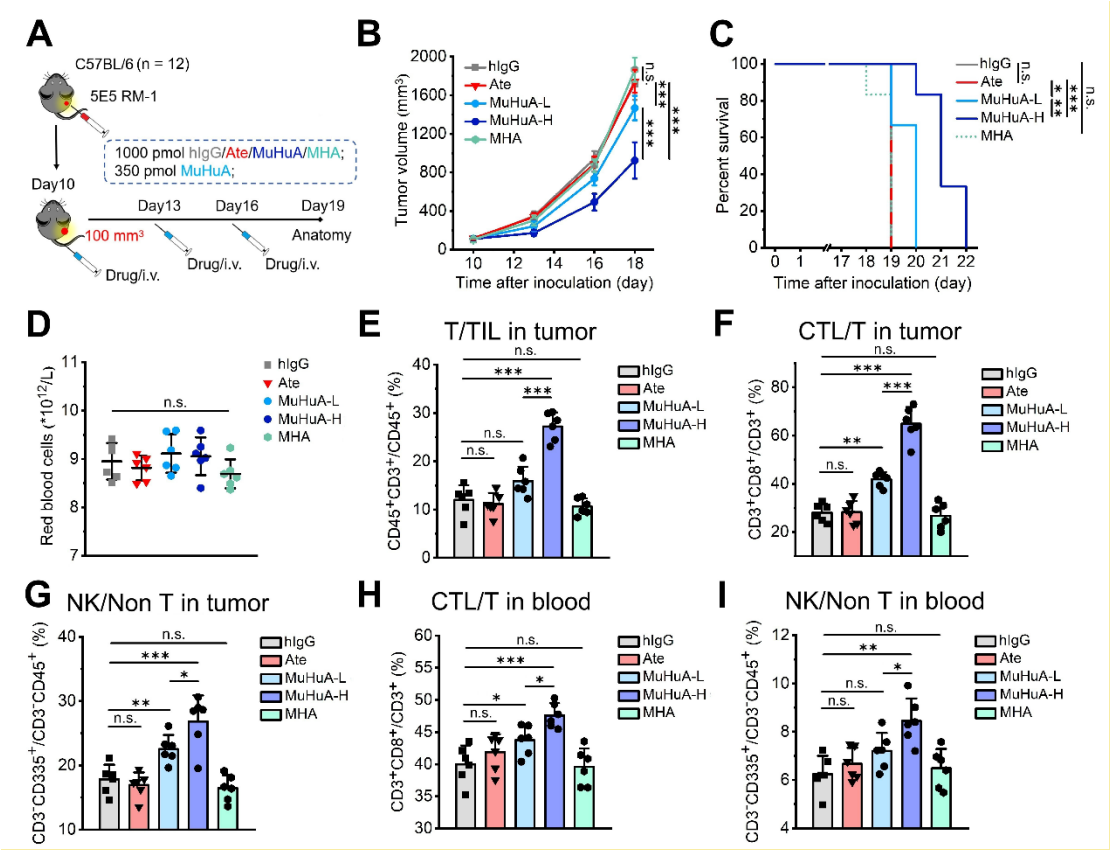


Figure 5. MuHuA overcomes ICIs resistance in cold tumors. (A) RM-1 study design. Tumor volume was tracked in 12 mice. When the control group reached the predefined endpoint, 6 animals were allocated for tumor weight measurement and flow cytometric analysis, while the remaining mice were followed for survival assessment. (B and C) Panel B illustrates the tumor-volume profiles across the treatment period, whereas panel C depicts the corresponding survival data, with 2000 mm³ defined as the endpoint (C). (D) Blood was obtained at the experimental endpoint, and RBC counts were measured by routine hematological analysis. (E-G) Flow-cytometric profiling of tumor-derived cells, including total T cells ($CD3^+$ among $CD45^+$ lymphocytes), $CD8^+$ T cells ($CD8^+$ within $CD45^+CD3^+$ cells), and NK cells ($CD335^+$ within $CD45^+CD3^-$ cells). (H-I) Peripheral blood lymphocytes were evaluated for the proportions of $CD8^+$ T cells and NK cells. Data are expressed as mean ± SD. *$p < 0.05$, **$p < 0.01$, ***$p < 0.001$; n.s.

indicates no statistical significance. Group comparisons were evaluated using an unpaired, two-sided Student's *t*-test. The log-rank (Mantel-Cox) test was used to assess survival.

MuHuA stimulates immune memory and suppresses tumor rechallenge

The superior therapeutic effect of MuHuA in the above experiments suggests its function in immune memory stimulation. We next examined whether treatment generated a durable systemic memory response (Figure 6A). As expected, MuHuA treatment increased the percentages of splenic $CD44^+$ T cells across both the MC38 and RM-1 models (Figure 6B, 6C, S10A, and S10B), indicating the establishment of immune memory. Additionally, splenocytes isolated from the mice in the MuHuA groups secreted greater amounts of IFN-γ after *in vitro* restimulation with MC38 or RM-1 cells (Figure 6D and 6E), confirming a strengthened memory immune response.

Mice were subsequently implanted subcutaneously with MC38 or RM-1 tumors on the right flank and received one administration of atezolizumab or MuHuA after the tumors reached approximately 100 mm^3. Tumors were resected upon reaching 300 mm^3, and 30 days after tumor removal, mice received a high-dose rechallenge with MC38 or RM-1 cells in the contralateral flank (Figure 6F). Notably, 4 of the 6 MuHuA & Surgery-treated mice remained tumor-free following MC38 rechallenge (Figure 6G and S10C), and all mice receiving MuHuA & Surgery showed marked suppression of RM-1 tumor growth after rechallenge (Figure 6H and S10D). To further evaluate the effect of MuHuA on the immune profile of TME, we analyzed intratumoral immune cell populations in MC38 and RM-1 tumor models (Figure S11A and S12A). MuHuA

exhibited potent tumor growth inhibition in both models, whereas the uPA inhibitor GGACK completely abolished its antitumor activity (Figure S11B&C and S12B&C). Additionally, MuHuA enriched intratumoral T cells and $CD8^+$ T cells compared to the atezolizumab group, while markedly reducing $CD4^+$ T cells and Tregs, consistent with the IF results (Figures S11D&E, S12D, and S13). These results indicate that MuHuA can be specifically cleaved by uPA within tumor tissues *in vivo* to restore its biological activity, and the systemic immune memory induced by a single injection of MuHuA can effectively reduce the growth of distant metastatic tumors, supporting the further development of MuHuA as a candidate for anticancer therapy.

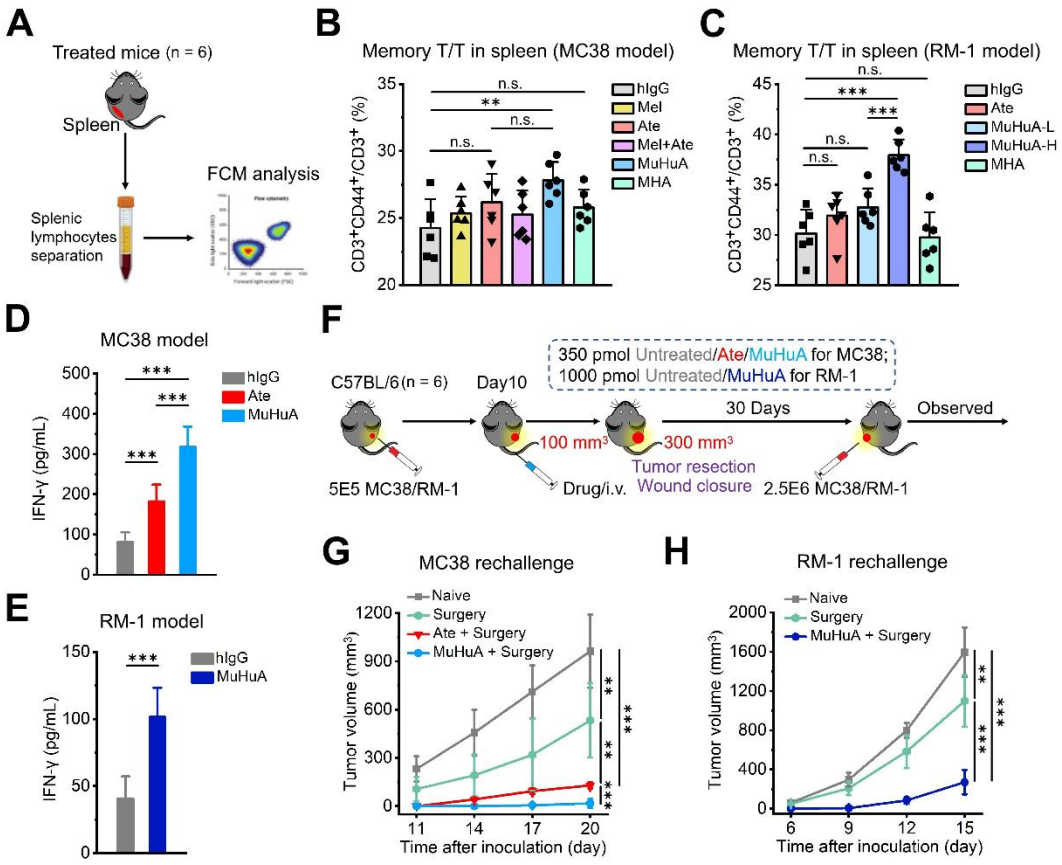


Figure 6. Preoperative MuHuA treatment suppresses tumor rechallenge. (A) Experimental scheme for splenic memory T cells analysis. (B and C) Splenic lymphocytes collected at the endpoints of the MC38 (B) and RM-1 (C) studies were

analyzed by FCM to quantify $CD44^+$ memory T cells among $CD45^+CD3^+$ T cells. (D and E) The isolated splenic lymphocytes of the MC38 (D) and RM-1 (E) model were restimulated with the corresponding mitomycin-C-treated tumor cells for 72 h, followed by ELISA quantification of IFN-γ in the culture supernatants. (F) Rechallenge study layout. (G and H) Growth of rechallenged MC38 (G) and RM-1 (H) tumors was tracked longitudinally. Data are expressed as mean ± SD. *$p < 0.05$, **$p < 0.01$, ***$p < 0.001$; n.s., not significant. Group comparisons were evaluated using an unpaired, two-sided Student's *t*-test.

The released melittin and atezolizumab synergize with each other in MuHuA therapy

To explore the mechanisms of action of MuHuA, we evaluated the synergistic effects between the released melittin and atezolizumab upon cleavage in the TME. MC38-bearing mice were administered three new constructs: HuR (R denotes rituximab), MuHuR, and HuA (Figure 7A). Upon cleavage, HuR releases rituximab alone, MuHuR releases both melittin and rituximab, and HuA releases atezolizumab alone, with rituximab not binding to any mouse proteins. As expected, HuR treatment showed no tumor inhibition (Figure 7B and S14A). Although MuHuR treatment had no evident side effects due to little hemolytic toxicity, it exhibited only minor tumor control (23% TGI). In contrast, HuA achieved a 36% TGI for the therapeutic effect of released atezolizumab. The MuHuA group, however, demonstrated significantly stronger tumor inhibition (77% TGI), far exceeding the combined efficacy observed with MuHuR and HuA. This group also achieved prolonged survival (Figure 7C, median survival: 37

635 days for MuHuA v.s. 30 days for HuA group), an increased proportion of intratumoral
636 $CD8^+$ T cells (Figure 7D) together with NK cells (Figure 7E), accompanied by greater
637 accumulation of both $CD8^+$ T cells and NK cells, alongside fewer intratumoral $CD4^+$ T
638 cell (Figure S14B). These results indicate a synergistic effect between melittin and
639 atezolizumab in MuHuA therapy. Additionally, qPCR analysis revealed that MuHuA
640 treatment significantly upregulated immune activation genes (*Ifng*, *Gzmb*, *Il12*, and
641 *Cxcl9*) and downregulated immune suppression genes (*Tgfb1*, *Il10*, and *Ccl5*) in tumor
642 tissue (Figure 7F and S14C).

643 To further investigate the synergistic effects between the released melittin and
644 atezolizumab, we incubated tumor cells with melittin and observed a significant release
645 of high mobility group box 1 (HMGB1), supporting melittin-induced immunogenic cell
646 death (ICD) (Figure 7G). It is well-established that PD-L1 upregulation confers
647 resistance to ICD. Supporting this, both MC38 and RM-1 cells exhibited marked
648 increases in PD-L1 expression after as short as 12 h of incubation with melittin (20 nM)
649 *in vitro* (Figure 7H). These findings suggest a possible synergistic mechanism: while
650 inducing ICD and promoting antigen exposure, melittin also upregulates tumor-cell PD-
651 L1 levels. Although such PD-L1 upregulation is generally considered an adaptive
652 resistance mechanism, it may also increase the availability of binding targets for PD-
653 L1-targeting antibodies and thereby enhance the response to PD-L1 blockade. Together,
654 these observations suggest that melittin and anti-PD-L1 antibodies may exert
655 synergistic antitumor effects through this mechanism.

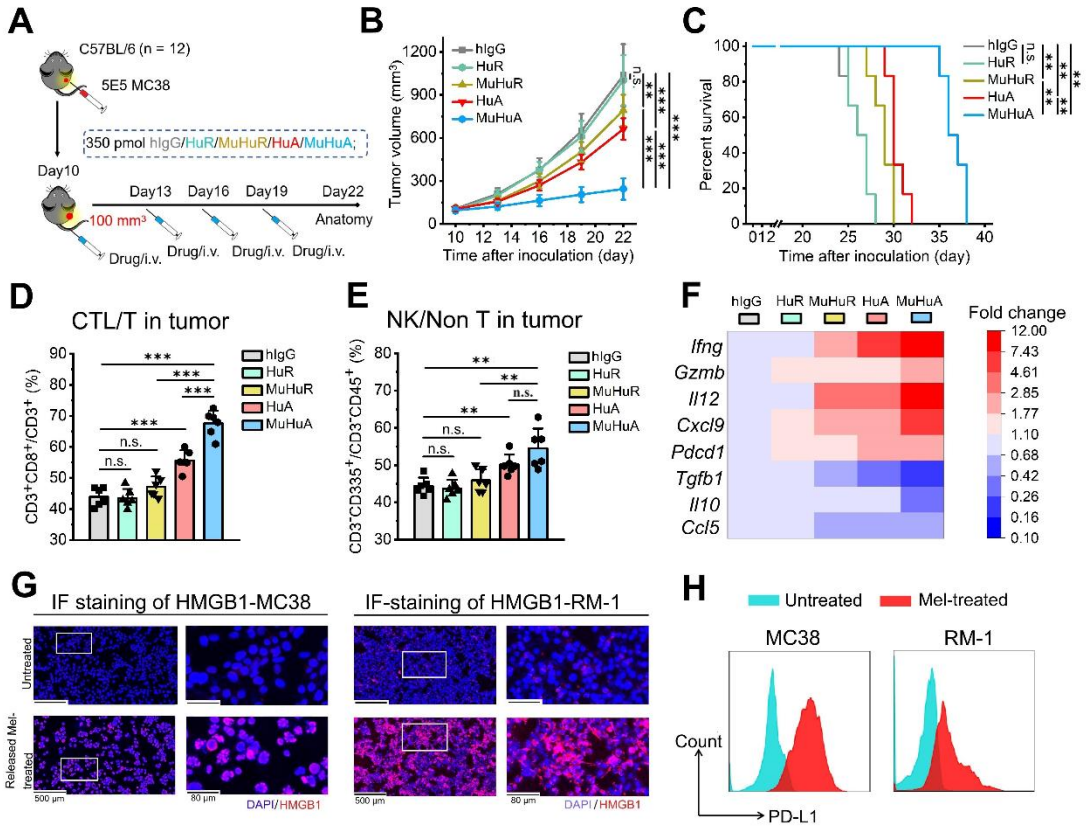


Figure 7. Synergistic effects of released melittin and atezolizumab in MuHuA therapy. (A) Study layout for the synergy experiment. Tumor volume was tracked in 12 mice. Once the control cohort reached the predefined endpoint, 6 animals were allocated for tumor weight determination and flow cytometric analysis, while the remaining animals were followed for survival assessment. (B and C) Changes in tumor burden throughout the observation period are presented in panel B, whereas the survival profiles of the treatment groups are shown in panel C, using 1500 mm³ as the endpoint. (D and E) Endpoint tumor-derived cells were evaluated. The percentages of $CD8^+$ T cells ($CD8^+$) within the total T-cell population ($CD45^+CD3^+$) (D) and NK cells ($CD335^+$) within the non-T-cell population ($CD45^+CD3^-$) (E) were evaluated by FCM. (F) Tumoral expression of several immune-related genes was quantified by qRT-PCR. (G) MC38 or RM-1 cells were exposed to 20 nM melittin for 24 h *in vitro*, followed by

detection of HMGB1 localization by IF staining. Scale bars, 500 μm for overview images and 80 μm for magnified images. (H) For PD-L1 analysis, MC38 and RM-1 cells received 20 nM melittin for 12 h *in vitro*, followed by detection of PD-L1 expression using FCM. Data are expressed as mean ± SD. *$p < 0.05$, **$p < 0.01$, ***$p < 0.001$; n.s., not significant. Comparisons were performed using an unpaired two-sided Student's *t*-test or One-Way ANOVA. Survival was assessed using the log-rank (Mantel-Cox) test.

MuHuA combined with CAR-T therapy exhibits enhanced efficacy and reduced toxicity compared to atezolizumab combination therapy

Leveraging the T cell-stimulating effects of MuHuA, we further explored its potential as a partner for chimeric antigen receptor T cell (CAR-T) therapy using an orthotopic HCC1954 human breast cancer model (Figure 8A).

Initially, we validated the lysis effect of melittin and confirmed the expression of EGFR on HCC1954 cells (Figure S15A and S15B). Then we generated EGFR-specific CAR-T cells for use as tumor-directed effector cells (Figure S15C and S15D). The results showed that MuHuA combined with EGFR CAR-T cells achieved more effective tumor suppression and caused less body weight loss compared to atezolizumab combination therapy (Figure 8B, 8C, and S15E). While no significant difference was observed in RBC counts (Figure 8D), the serum ALT levels were notably higher in the EGFR CAR-T & atezolizumab group (Figure 8E). Combining EGFR CAR-T cells with atezolizumab, but not with MuHuA, led to significant peripheral on-target toxicity, reflected by increased serum ALT, hepatic injury confirmed by H&E

staining (Figure S15F), and a significantly higher serum IFN-γ level (Figure 8F). Conversely, combining EGFR CAR-T cells with MuHuA markedly increased intratumoral IFN-γ levels (Figure 8G). Moreover, caspase-3 activation in tumor tissues was significantly enhanced in this group (Figure 8H), without causing evident damage to peritumoral normal breast tissue (Figure S15G), possibly due to the melittin released from MuHuA. Further FCM analysis (Figure S15H) and IF staining showed greater representation of intratumoral EGFR CAR-T cells and mouse endogenous myeloid cells within the EGFR CAR-T & MuHuA group (Figure 8I-K and S15I).

In summary, MuHuA significantly enhanced the tumor-suppressive activity of CAR-T treatment without exacerbating its toxicity on normal tissues, suggesting a more favorable tumor-specific immune response.

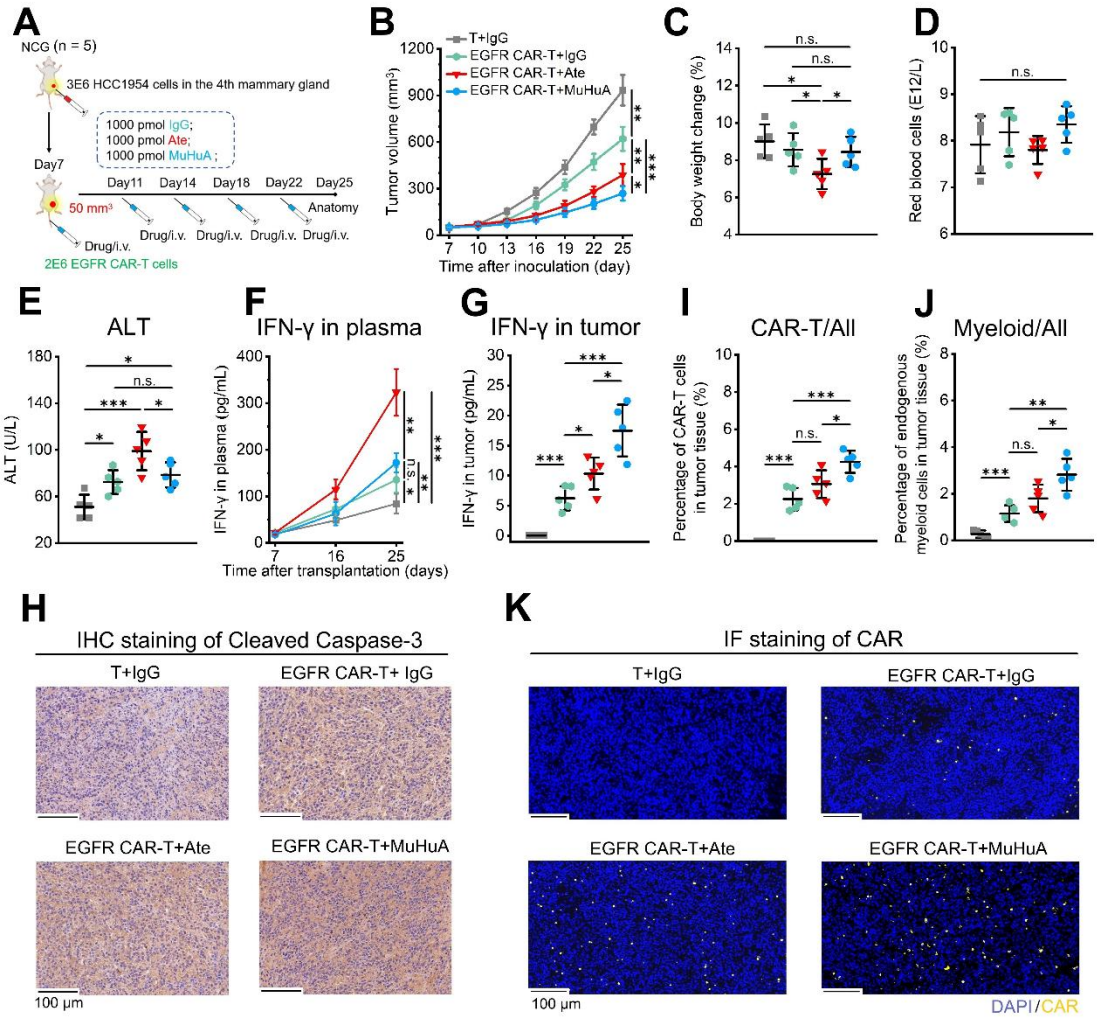


Figure 8. MuHuA improves CAR-T-mediated tumor control without additional toxicity. (A) Orthotopic HCC1954 breast tumor study layout. (B) Tumor growth was tracked longitudinally. (C-E) Body weight change was measured at the endpoint (C). Blood samples were collected on the same day. RBC counts were determined by routine blood test (D), and plasma ALT levels were detected by biochemistry analysis (E). (F and G) IFN-γ concentrations in serum (F) and tumor tissue (G) were determined by ELISA. (H) Tumoral cleaved caspase-3 abundance was assessed by IHC staining. Scale bars, 100 μm. (I and J) Endpoint tumor-derived cells were subjected to FCM to quantify EGFR CAR-T cells (CAR+) (I) and endogenous mouse myeloid cells ($CD45^+$) (J). (K) The proportions of CAR-T cells in tumor tissues were evaluated using IF staining. Scale

bars, 100 μm. Data are expressed as mean ± SD. *$p < 0.05$, **$p < 0.01$, ***$p < 0.001$; n.s., not significant. Comparisons were performed using an unpaired two-sided Student's *t*-test or One-Way ANOVA.

Discussion

ICIs have demonstrated prolonged survival benefits for patients with various tumor types, yet their immunostimulatory effects on healthy tissues can cause toxicity. Accordingly, patients with pre-existing autoimmune disorders are frequently underrepresented in ICIs clinical trials, despite their increased cancer risk [39, 40]. Another concern is their unsatisfactory pharmacokinetic profiles and biodistribution. High accumulation of intravenously injected atezolizumab has been observed in the spleen, lungs, liver, kidneys, and heart of mice, cynomolgus macaques, and human patients [41, 42]. This widespread distribution significantly contributes to irAEs, primarily due to the presence of PD-L1, its cognate ligand, across multiple normal cell types [43]. Here, our dual-lock design of MuHuA successfully enhanced tumor-targeting capabilities compared to the parent atezolizumab (Figure 3D), thereby effectively mitigating the immune-related risks associated with systemic atezolizumab administration (Figure 2).

Though melittin has gained attention because of its ability to lyse diverse tumor cells, its intravenous administration induces potent hemolysis, severely hampering its clinical applications. Worse still, the reduced oxygen supply in the TME caused by hemolysis can lead to immune effector cell dysfunction and decreased

736 immunotherapy effectiveness [44, 45]. Nanoparticle is among the most intensively
737 studied solutions to this issue. However, melittin-loaded nanoparticles still retain
738 partial hemolytic activity and nonspecific cytotoxicity due to accidental release and
739 hepatic uptake [46]. The proposed lytic steps of melittin involve aggregation on the
740 membrane driven by electrostatic interactions, assembly on the membrane bilayer,
741 membrane insertion, and eventual lysis with increasing peptide concentration [47, 48].
742 Fusion with a large protein can effectively abrogate melittin's hemolytic activity, as it
743 dramatically restricts its physical freedom and significantly impacts all these steps
744 [49]. In this study, the fusion of melittin with a hinge and atezolizumab in MuHuA
745 substantially reduces its membrane-disrupting capacity, markedly enhancing its safety
746 (Figure 1).

747 After confirming efficient masking and good *in vivo* tolerability of MuHuA, we
748 proceeded to evaluate its therapeutic efficacy against tumors. Significantly improved
749 antitumor effects have been achieved by combining PD-1/PD-L1 inhibitors with other
750 treatments, such as chemotherapy, radiotherapy, kinase inhibitors, or oncolytic
751 virotherapy [50, 51]. In this work, combining melittin with atezolizumab dramatically
752 enhanced antitumor activity (Figure 4 B and C), and MuHuA treatment further
753 improved therapeutic efficacy and modestly prolonged survival in both hot and cold
754 tumor models (for hot tumor models: 34 days for MuHuA and 28 days for Ate; for cold
755 tumor models: 21 days for MuHuA-H and 19 days for Ate) (Figure 4 and 5). Notably,
756 MuHuA treatment established robust and durable immune memory, effectively
757 suppressing tumor rechallenge (Figure 6G, 6H and S10). Because PD-1/PD-L1

blockade depends substantially on an existing antitumor immune response, its therapeutic activity is frequently attenuated in poorly infiltrated tumors, including cold and advanced-stage lesions. In these settings, melittin released from MuHuA effectively re-initiates the immune cycle and enhances the antitumor activity of atezolizumab (Figure 5 and S8).

Mechanistically, MuHuA induces tumor cell lysis via released melittin and promotes a tumor-directed immune response marked by significantly greater intratumoral accumulation and activation of $CD8^+$ T cells and NK cells (Figure 4E-G and 5E-G), along with a Th1-polarized tumor microenvironment (Figure 7F and S14C). Additionally, similar to therapeutic agents such as gemcitabine and TLR7 agonists, melittin markedly upregulates PD-L1 abundance in tumor cells. At sufficiently high doses, this phenomenon has been associated with durable benefit from PD-1/PD-L1 inhibition and favorable clinical outcomes [52, 53]. Our dual-lock strategy enables MuHuA to be administered at doses significantly higher than those tolerated for atezolizumab (Figure 2C), thereby ensuring robust blockade of PD-1/PD-L1 and profound efficacy. Furthermore, melittin released within tumors preferentially binds tumor cells rather than immune cells, likely due to the higher membrane cholesterol content of tumor cells [54], which explains the enhanced effectiveness of EGFR CAR-T cells in combination with MuHuA (Figure 8). Notably, melittin has also been reported to increase TNF-α release while reducing IL-10 secretion from macrophages, further supporting its immunomodulatory role [55]. Overall, MuHuA is a novel construct designed to harness the synergistic antitumor effects of ICI and cell-lytic peptides.

Although the melittin/atezolizumab dual-lock prodrug shows a favorable safety profile and potent antitumor efficacy, its efficacy depends on efficient cleavage within tumor tissues. In this study, we employed uPA as the trigger for melittin and atezolizumab release. Several tumor-associated extracellular proteases, including uPA and MMPs, are commonly enriched in malignant tumors [56]. Compared with the complex and functionally redundant MMP family, the uPA/uPAR axis represents a more defined proteolytic pathway and acts upstream of the plasminogen–plasmin–MMP cascade making uPA an attractive trigger for tumor-selective therapeutic activation [57]. Accordingly, uPA-responsive sequences such as LSGRSDNH, identified through the cellular libraries of peptide substrates (CLiPS) based combinatorial screening and counterselection strategy, have been widely used in the development of probody therapeutics, tumor-selective ADCs, and cytokine prodrug platforms [58].

Nevertheless, the choice of activating protease remains an important but unresolved challenge in tumor-activated prodrug design. In this study, uPA was selected as a representative protease to establish and validate the feasibility of the dual-lock design strategy, rather than to suggest that it is universally optimal for all tumor settings. Moreover, protease expression and activity can vary across tumor types and among individual patients. Future applications of this platform may require the establishment of protease expression patterns, supported by broader tumor tissue profiling or personalized evaluation of protease activity.

The current dual-lock prodrug design also has limitations. For example, the four extra amino acids remaining at the C-terminus of melittin after uPA cleavage partially impairs its pore-forming capacity. Therefore, exploring alternative tumor-associated proteases with more efficient cleavage or shorter residual sequences will be essential. Furthermore, other agonist antibodies associated with substantial immune toxicity, such as anti-CD3, anti-41BB, and anti-OX40 antibodies, should be incorporated into the dual-lock platform to verify its universality [59]. Lastly, given that our studies were conducted in cell line-derived tumor models, the clinical potential of MuHuA should be further evaluated in patient-derived tumors using humanized mouse models.

Conclusions

In summary, we present the first tumor-specific melittin/atezolizumab dual-lock prodrug. This design effectively masks both melittin and atezolizumab, thereby reducing hemolysis and irAEs by selectively delivering the active agents to tumors. Overall, this strategy not only overcomes resistance to immune checkpoint inhibitors and improves efficacy in cold tumors, but also enables the safe therapeutic use of melittin. It lays the groundwork for future developments of prodrugs that combine active peptides with immune-modulating antibodies.

Abbreviations

ICIs: Immune checkpoint inhibitors; irAEs: immune-related adverse events; MuHuA: tumor-specific melittin/atezolizumab dual-lock prodrug; PD-1: programmed cell death protein 1; PD-L1: Programmed Death-Ligand 1; TME: tumor microenvironment; ACPs:

anticancer peptides; uPA: urokinase-type plasminogen activator; DMEM: Dulbecco's Modified Eagle's Medium; FBS: fetal bovine serum; BSA: bovine serum albumin; OCT: optimal cutting temperature; H&E: hematoxylin and eosin; TGI: Tumor Growth Inhibition; RPMI: Roswell Park Memorial Institute; RBCs: red blood cells; ALT: alanine aminotransferase; AST: aspartate aminotransferase; EC50: half-maximal effective concentration; NOD: Non-Obese Diabetes mice; AUC: area under the curve; T 1/2α: distribution half-life; FCM: flow cytometry; IHC: Immunohistochemistry; TILs: tumor-infiltrating lymphocytes; HIF1α: hypoxia-inducible factor 1α; ICD: immunogenic cell death; HMGB1: high mobility group box 1; CAR-T: chimeric antigen receptor T cell.

Supplementary Material

The following is the Supporting Information to this article:

Acknowledgements

Funding

The work was supported by the National Natural Science Foundation of China (No.82504648 to Dr. Zhu W, No. 82570646 to Dr. Jiang, No. 82574302, W2412118, and 22494694 to Dr. Lu H), Opening Foundation of National Engineering Research Center of Genetic Medicine (No. NERCGM-OF-20250401 to Dr. Lu H), and Shanghai Key Laboratory for Antibody-Drug Conjugates with Innovative Target (Grant No. 24dz2261300 to Dr. Lu H).

Authorship contribution statement

Wen Zhu: Conceptualization, Data curation, Formal analysis, Funding acquisition, Investigation, Methodology, Project administration, Resources, Software, Validation, Writing - original draft, and Writing - review & editing. Ying Qin: Data curation and Validation. Yuntian Han: Data curation and Validation. Gen Qi: Data curation and Validation. Qiongya Zeng: Data curation and Validation. Zixiang Li: Data curation and Validation. Haoran Deng: Data curation and Validation. Xinyu Deng: Data curation and Validation. Kaijuan Yi: Data curation and Validation. Yan Wang: Writing - review & editing. Anja Moldenhauer: Writing - review & editing. Shanshan Jiang: Funding acquisition and Writing - review & editing. Huili Lu: Conceptualization, Supervision, Funding acquisition, Writing - original draft, and Writing - review & editing.

Data availability statement

All data supporting the findings of this study are available from the lead contact upon reasonable request. Additional inquiries regarding resources or reagents should be addressed to the lead contact, Huili Lu (roadeer@sjtu.edu.cn).

AI tool disclosure

No artificial intelligence tools were used in the manuscript preparation, image generation, data collection, and data analysis processes.

Competing Interests

The authors have declared that no competing interest exists.

Ethics Approval Statement

The mice in the study were handled according to guidelines from the Institutional Animal Care and Use Committee of Shanghai Jiao Tong University (Ethics number: 202501162).

References

1. Roussot N, Kaderbhai C, Ghiringhelli F. Targeting immune checkpoint inhibitors for non-small-cell lung cancer: beyond PD-1/PD-L1 monoclonal antibodies. Cancers (Basel). 2025; 17, 906.
2. Zhang K, Kong X, Li Y, Wang Z, Zhang L, Xuan L. PD-1/PD-L1 inhibitors in patients with preexisting autoimmune diseases. Front Pharmacol. 2022; 13: 854967.
3. Naing A, McKean M, Rosen LS, Sommerhalder D, Shaik NM, Wang IM, et al. First-in-human phase I study to evaluate safety, tolerability, pharmacokinetics, pharmacodynamics, immunogenicity, and antitumor activity of PF-07209960 in patients with advanced or metastatic solid tumors. ESMO Open. 2025; 10: 104291.
4. Socinski MA, Jotte RM, Cappuzzo F, Nishio M, Mok TSK, Reck M, et al. Association of immune-related adverse events with efficacy of atezolizumab in patients with non-small cell lung cancer: pooled analyses of the phase 3 IMpower130, IMpower132, and IMpower150 randomized clinical trials. JAMA Oncol. 2023; 9: 527–35.
5. Cheng C, Wang Q, Zhang S. Synergy of oncolytic adenovirus and immune checkpoint inhibitors: transforming cancer immunotherapy paradigms. Front Immunol. 2025; 16: 1610858.
6. Desbois M, Giffon T, Yakkundi P, Denson CR, Sekar K, Hart KC, et al. IGM-7354, an immunocytokine with IL15 fused to an anti-PD-L1 IgM, induces NK and CD8+ T cell-mediated cytotoxicity of PD-L1-positive tumor cells. Cancer Immunol Res. 2025; 13: 1172–89.
7. Autio KA, Boni V, Humphrey RW, Naing A. Probody therapeutics: an emerging class of therapies designed to enhance on-target effects with reduced off-tumor toxicity for use in immuno-oncology. Clin Cancer Res. 2020; 26: 984–9.
8. Liang Y, Wang B, Chen Q, Fu X, Jiang C, Lin Z, et al. Systemic delivery of glycosylated-PEG-masked oncolytic virus enhances targeting of antitumor immuno-virotherapy and modulates T and NK cell infiltration. Theranostics. 2023; 13: 5452–68.
9. Lo BC, Kryczek I, Yu J, Vatan L, Caruso R, Matsumoto M, et al. Microbiota-dependent activation of CD4+ T cells induces CTLA-4 blockade–associated colitis via Fcγ receptors. Science. 2024; 383: 62–70.
10. Paul S, Konig MF, Pardoll DM, Bettegowda C, Papadopoulos N, Wright KM, et al. Cancer therapy with antibodies. Nat Rev Cancer. 2024; 24: 399–426.
11. Tsuchikama K, Anami Y, Ha SYY, Yamazaki CM. Exploring the next generation of antibody-drug conjugates. Nat Rev Clin Oncol. 2024; 21: 203–23.
12. Dumontet C, Reichert JM, Senter PD, Lambert JM, Beck A. Antibody-drug conjugates come of age in oncology. Nat Rev Drug Discov. 2023; 22: 641–61.
13. Mansurov A, Hosseinchi P, Chang K, Lauterbach AL, Gray LT, Alpar AT, et al. Masking the immunotoxicity of interleukin-12 by fusing it with a domain of its receptor via a tumour-protease-cleavable linker. Nat Biomed Eng. 2022; 6: 819–29.
14. Etxeberria I, Bolaños E, Teijeira A, Garasa S, Yanguas A, Azpilikueta A, et al. Antitumor efficacy and reduced toxicity using an anti-CD137 Probody therapeutic. Proc Natl Acad Sci U S A. 2021; 118: e2025930118.
15. Xing J, Lu W, Zhang Y, Yang C, Yang J, Shi J, et al. Design of prodrugs with reactive oxygen species as activators and their application in tumor therapy. Theranostics. 2026; 16: 1295–327.
16. Deng A, Fan R, Hai Y, Zhuang J, Zhang B, Lu X, et al. A STING agonist prodrug reprograms tumor-associated macrophage to boost colorectal cancer immunotherapy. Theranostics. 2025; 15: 277–99.
17. Desnoyers LR, Vasiljeva O, Richardson JH, Yang A, Menendez EE, Liang TW, et al. Tumor-specific

activation of an EGFR-targeting probody enhances therapeutic index. Sci Transl Med. 2013; 5: 207ra144.
18. Jhunjhunwala S, Hammer C, Delamarre L. Antigen presentation in cancer: insights into tumour immunogenicity and immune evasion. Nat Rev Cancer. 2021; 21: 298–312.
19. Hu Y, Tang L, Kuang Z, Huang D, Li T, Yin G, et al. Mutual exclusion analysis shows that DUSP9 negatively regulates PD-L1 expression and acts as a target to enhance anti-PD-1 efficacy. Adv Sci (Weinh). 2025: e14347.
20. Wu M, Huang Q, Xie Y, Wu X, Ma H, Zhang Y, et al. Improvement of the anticancer efficacy of PD-1/PD-L1 blockade via combination therapy and PD-L1 regulation. J Hematol Oncol. 2022; 15: 24.
21. Chen R, Li Z, Fang Z, Li Z, Yang D, Li Y, et al. Chemotherapy-mediated induction of PD-L1 via SEI1 facilitates myeloma immune evasion. Adv Sci (Weinh). 2025; 12: e2411082.
22. Ma Y, Liu X, Zhang X, Yu Y, Li Y, Song M, et al. Efficient mining of anticancer peptides from gut metagenome. Adv Sci (Weinh). 2023; 10: e2300107.
23. Ghadiri N, Javidan M, Sheikhi S, Taştan Ö, Parodi A, Liao Z, et al. Bioactive peptides: an alternative therapeutic approach for cancer management. Front Immunol. 2024; 15: 1310443.
24. Rady I, Siddiqui IA, Rady M, Mukhtar H. Melittin, a major peptide component of bee venom, and its conjugates in cancer therapy. Cancer Lett. 2017; 402: 16–31.
25. Rocha MM, Dariva I, Zornoff GC, De Laurentis GS, Mendes GC, Santana MG, et al. A new therapeutic approach for bone metastasis in colorectal cancer: intratumoral melittin. J Venom Anim Toxins Incl Trop Dis. 2022; 28: e20210067.
26. Zhang HQ, Sun C, Xu N, Liu W. The current landscape of the antimicrobial peptide melittin and its therapeutic potential. Front Immunol. 2024; 15: 1326033.
27. Yu X, Jia S, Yu S, Chen Y, Zhang C, Chen H, et al. Recent advances in melittin-based nanoparticles for antitumor treatment: from mechanisms to targeted delivery strategies. J Nanobiotechnology. 2023; 21: 454.
28. Hoshino Y, Koide H, Furuya K, Haberaecker WW, 3rd, Lee SH, Kodama T, et al. The rational design of a synthetic polymer nanoparticle that neutralizes a toxic peptide in vivo. Proc Natl Acad Sci U S A. 2012; 109: 33–8.
29. Ye R, Zheng Y, Chen Y, Wei X, Shi S, Chen Y, et al. Stable loading and delivery of melittin with lipid-coated polymeric nanoparticles for effective tumor therapy with negligible systemic toxicity. ACS Appl Mater Interfaces. 2021; 13: 55902–12.
30. Zhu W, Qin Y, Han Y, Qi G, Zeng Q, Song L, et al. A RGD-directed melittin/anti-41BB dual-lock prodrug safely reinvigorates robust anti-tumor immunity. Molecular Therapy. 2026. In press. Article identifier: S1525001626008609. DOI: 10.1016/j.ymthe.2026.09.041.
31. Jia S, Chen Y, Zhuo C, Hu M, Zhang C, Cai H, et al. Aptamer-modified melittin micelles efficiently inhibit osteosarcoma deterioration by inducing immunogenic cell death. Colloids and Surfaces B: Biointerfaces. 2025; 249: 114512.
32. Qin Y, Han Y, Qi G, Tang J, Dong X, Sun J, et al. Engineering energy metabolism boosts therapeutic protein production via the E. coli hemolysin A system. TransMed. 2026; 1: 100014.
33. Shi W, Lv L, Liu N, Wang H, Wang Y, Zhu W, et al. A novel anti-PD-L1/IL-15 immunocytokine overcomes resistance to PD-L1 blockade and elicits potent antitumor immunity. Mol Ther. 2023; 31: 66–77.
34. Zhu W, Wang Y, Lv L, Wang H, Shi W, Liu Z, et al. Universal chimeric Fcγ receptor T cells with appropriate affinity for IgG1 antibody exhibit optimal antitumor efficacy. Acta Pharm Sin B. 2023; 13: 2071–85.
35. Ferris ST, Liu T, Chen J, Ohara RA, Ou F, Wu R, et al. WDFY4 deficiency in NOD mice ameliorates

autoimmune diabetes and insulitis. Proc Natl Acad Sci U S A. 2023; 120: e2219956120.
36. Chester C, Sanmamed MF, Wang J, Melero I. Immunotherapy targeting 4-1BB: mechanistic rationale, clinical results, and future strategies. Blood. 2018; 131: 49–57.
37. Jeong S, Park E, Kim HD, Sung E, Kim H, Jeon J, et al. Novel anti-4-1BB×PD-L1 bispecific antibody augments anti-tumor immunity through tumor-directed T-cell activation and checkpoint blockade. J Immunother Cancer. 2021; 9: e002428.
38. Gao J, Wang Z, Jiang W, Zhang Y, Meng Z, Niu Y, et al. CLDN18.2 and 4-1BB bispecific antibody givastomig exerts antitumor activity through CLDN18.2-expressing tumor-directed T-cell activation. J Immunother Cancer. 2023; 11: e006704.
39. Wong PY, How SH, Ismail I, Hassan R. Single dose of atezolizumab plus chemotherapy in active psoriasis with advanced non-small cell lung cancer. J Oncol Pharm Pract. 2022; 28: 471–4.
40. Cheng J, Cai M, Wang G. Incidence and relative risk of colorectal cancer in autoimmune diseases: a global pooled-analysis with more than 91 million participants. Int J Surg. 2025; 111: 7236–42.
41. Giesen D, Broer LN, Lub-de Hooge MN, Popova I, Howng B, Nguyen M, et al. Probody therapeutic design of (89)Zr-CX-072 promotes accumulation in PD-L1-expressing tumors compared to normal murine lymphoid tissue. Clin Cancer Res. 2020; 26: 3999–4009.
42. Bensch F, van der Veen EL, Lub-de Hooge MN, Jorritsma-Smit A, Boellaard R, Kok IC, et al. (89)Zr-atezolizumab imaging as a non-invasive approach to assess clinical response to PD-L1 blockade in cancer. Nat Med. 2018; 24: 1852–8.
43. Doroshow DB, Bhalla S, Beasley MB, Sholl LM, Kerr KM, Gnjatic S, et al. PD-L1 as a biomarker of response to immune-checkpoint inhibitors. Nat Rev Clin Oncol. 2021; 18: 345–62.
44. Pal M, Bao W, Wang R, Liu Y, An X, Mitchell WB, et al. Hemolysis inhibits humoral B-cell responses and modulates alloimmunization risk in patients with sickle cell disease. Blood. 2021; 137: 269–80.
45. Ma S, Zhao Y, Lee WC, Ong LT, Lee PL, Jiang Z, et al. Hypoxia induces HIF1α-dependent epigenetic vulnerability in triple negative breast cancer to confer immune effector dysfunction and resistance to anti-PD-1 immunotherapy. Nat Commun. 2022; 13: 4118.
46. Tang L, Li Y, Lv X, Guo J, Zhang Y, Lin Y, et al. Redox-responsive polymeric nanocapsules for enhanced tumor-targeted delivery of antimicrobial peptides. Adv Sci (Weinh). 2026; 13: e74480.
47. Hong J, Lu X, Deng Z, Xiao S, Yuan B, Yang K. How melittin inserts into cell membrane: conformational changes, inter-peptide cooperation, and disturbance on the membrane. Molecules. 2019; 24: 1775.
48. Jamasbi E, Mularski A, Separovic F. Model membrane and cell studies of antimicrobial activity of melittin analogues. Curr Top Med Chem. 2016; 16: 40–5.
49. Zhu W, Wang Y, Lv L, Wang H, Shi W, Liu Z, et al. SHTXTHHly, an extracellular secretion platform for the preparation of bioactive peptides and proteins in Escherichia coli. Microb Cell Fact. 2022; 21: 128.
50. Villacampa G, Navarro V, Matikas A, Ribeiro JM, Schettini F, Tolosa P, et al. Neoadjuvant immune checkpoint inhibitors plus chemotherapy in early breast cancer: a systematic review and meta-analysis. JAMA Oncol. 2024; 10: 1331–41.
51. Li Z, Li M, Yang L, Chen J, Ye Q, Qian W, et al. Oncolytic vaccinia virus armed with anti-CD47 nanobody elicit potent antitumor effects on multiple tumor models via enhancing innate and adoptive immunity. J Immunother Cancer. 2024; 12: e009473.
52. Peng J, Hamanishi J, Matsumura N, Abiko K, Murat K, Baba T, et al. Chemotherapy induces programmed cell death-ligand 1 overexpression via the nuclear factor-κb to foster an immunosuppressive

tumor microenvironment in ovarian cancer. Cancer Res. 2015; 75: 5034–45.
53. Yu X, Long Y, Chen B, Tong Y, Shan M, Jia X, et al. PD-L1/TLR7 dual-targeting nanobody-drug conjugate mediates potent tumor regression via elevating tumor immunogenicity in a host-expressed PD-L1 bias-dependent way. J Immunother Cancer. 2022; 10: e004590.
54. Britt HM, Mosely JA, Sanderson JM. The influence of cholesterol on melittin lipidation in neutral membranes. Phys Chem Chem Phys. 2019; 21: 631–40.
55. Jeong C, Kim J, Han IH, Kim S, Choi I, Kim H, et al. Melittin derived peptide-drug conjugate, M-DM1, inhibits tumor progression and induces effector cell infiltration in melanoma by targeting M2 tumor-associated macrophages. Front Immunol. 2023; 14: 1178776.
56. Zhai B-T, Tian H, Sun J, Zou J-B, Zhang X-F, Cheng J-X, et al. Urokinase-type plasminogen activator receptor (uPAR) as a therapeutic target in cancer. Journal of Translational Medicine. 2022; 20: 135.
57. El Salamouni NS, Buckley BJ, Ranson M, Kelso MJ, Yu H. Urokinase plasminogen activator as an anti-metastasis target: inhibitor design principles, recent amiloride derivatives, and issues with human/mouse species selectivity. Biophys Rev. 2022; 14: 277–301.
58. Lin WW, Lu YC, Chuang CH, Cheng TL. Ab locks for improving the selectivity and safety of antibody drugs. J Biomed Sci. 2020; 27: 76.
59. van Winkel CAJ, Fan X, Giesen D, Gauderat G, de Jong S, Jaquin T, et al. Elevated target expression by dual PD-L1 and 4-1BB engagement is associated with (89)Zr-PD-L1x4-1BB bispecific Mabcalin tumor uptake. Theranostics. 2026; 16: 6184–201.